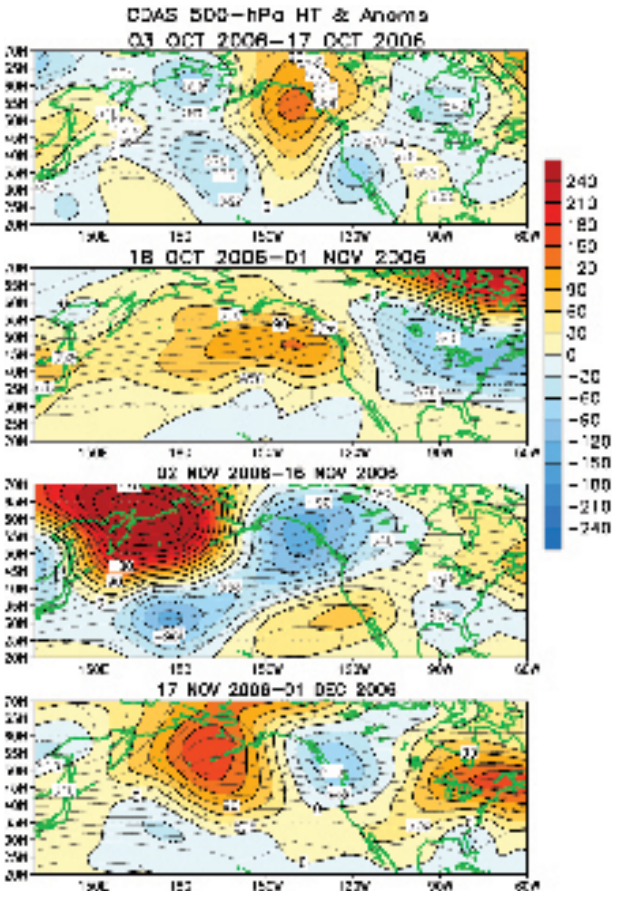

Fig. 2.27. 500-hPa heights (dm) and anomalies (m) over the North Pacific and North America during the 2-week periods indicated on each panel.

replaced by a persistent blocking pattern that developed over the high latitudes of the west-central North Pacific in early November (Fig. 2.27). The northern and southern branches of the Pacific jet stream recombined over the eastern North Pacific, contributing to a series of strong storms that resulted in remarkably wet and cold conditions in the Pacific Northwest, western Canada, and portions of Alaska during the first half of November 2006. This pattern projected very strongly on the negative phase of the WP teleconnection pattern during November 2006 (Fig. 2.23b).

It is important to note that the conditions during November 2006 were related to midlatitude variability, with little or no connection to the developing El Niño conditions in the tropical Pacific. In particular, these events occurred in advance of the development of El Niño–related enhanced convection near and to the east of the international date line, which typically leads to atmospheric coupling and an eastward shift of the subtropical ridges and the North Pacific jet stream during the NH winter.

3. GLOBAL OCEANS—J. M. Levy, Ed.

a. Overview—J. M. Levy

As the global ocean observing system matures, climatologies of essential climate variables are growing more robust, as are observations of anomalous departures that shed light on the evolving behavior of the coupled ocean–atmosphere system. Year 2006 exhibited numerous anomalies of interest:

- Global SST anomalies were primarily positive, notably so in boreal summer in the North Atlantic and in the latter part of the year in the central and eastern equatorial Pacific, associated with the 2006 El Niño.
- The mean of latent plus sensible heat flux was similar to that in 2005; total flux in both years was at the high end of a long-term upward trend that started in 1977/78. Significant heat flux anomalies were observed in the regions of the 2006 El Niño and Indian Ocean dipole mode event.
- Global sea surface salinity anomalies accentuated climatological patterns: freshwater regions were fresher and salty regions were saltier. The subpolar North Atlantic and Nordic Seas were anomalously salty in 2006.
- Dramatic westward surface current anomalies associated with the development of El Niño were observed late in the year in the tropical Pacific Ocean, while the seasonal reversal of currents was particularly pronounced on the equator in the Atlantic Ocean. Exchange of water between the South and North Atlantic Oceans was weaker than normal.
- The MOC in the North Atlantic was a bit low, albeit within a standard deviation of the historical annual mean. However, there is no indication of a systematic trend in MOC transport.
- Annual mean SLA was above the 1993–99 baseline average for nearly 80% of the ocean. The global mean SLA change of +6 mm from 2005 was the highest increase since the altimeter record began in 1993. Relative sea level change was also the highest ever recorded. There were an anomalously high number of extreme sea level events.
- Global ocean carbon uptake in 2005 (about 2.2 Pg C yr^{-1}) was near average for the past decade. Interannual variability over the past decade has been about ±0.2 Pg C yr^{-1}. Atlantic Ocean anthropogenic CO_2 uptake continues to exceed Pacific Ocean uptake.
- Global annual average ocean color anomalies were not markedly different from those observed in the satellite record over the past decade. However,

anomalies in the Niño-3.4 region were indicative of a 2006 El Niño that was stronger (considerably weaker) than that of 2002/03 (1997/98).

b. Temperature

1) Sea surface temperature—R. W. Reynolds

SSTs for 2006 are shown as monthly fields interpolated from the weekly 1° OI analyses of Reynolds et al. (2002). All results presented here are depicted as anomalies defined as differences from a 1971–2002 climatological base period described by Xue et al. (2003).

The yearly average and standard deviation of the monthly anomalies are shown in Fig. 3.1. The anomalies are primarily positive resulting from overall global warming relative to the climatological base period. Three features dominate 2006. First, the average shows a strong positive anomaly signal in the North Atlantic and North Pacific between roughly 40° and 65°N. This is due to a boreal summer positive anomaly, which also occurred in 2003–06. However, in 2006, the summer anomaly in the Pacific was relatively weak compared with 2003–05. Second, in 2005 there was also a strong positive anomaly of roughly 1°C in the tropical North Atlantic (0°–30°N) while in 2006 it was smaller. Finally, a weak El Niño began to be evident in June (see section 4).

The zonally averaged monthly anomaly is shown for the Atlantic between 80°W and 20°E for 2000–06 in Fig. 3.2. Strong positive summer anomalies are shown north of 40°N beginning in 2003. The anomaly signals were the oceanic response to summer heat waves that helped reduce summer ice cover in the Arctic. The 2003 European summer heat wave corresponded to an especially strong positive SST anomaly. In addition, the 2005 spring and summer tropical North Atlantic positive anomalies are evident between 5° and 20°N in the figure and were smaller in 2006. The smaller anomalies in 2006 may partly explain the lower number of 2006 Atlantic hurricanes compared to 2005.

2) Heat content—G. C. Johnson, J. M. Lyman, and J. K. Willis

Storage and transport of heat in the ocean are

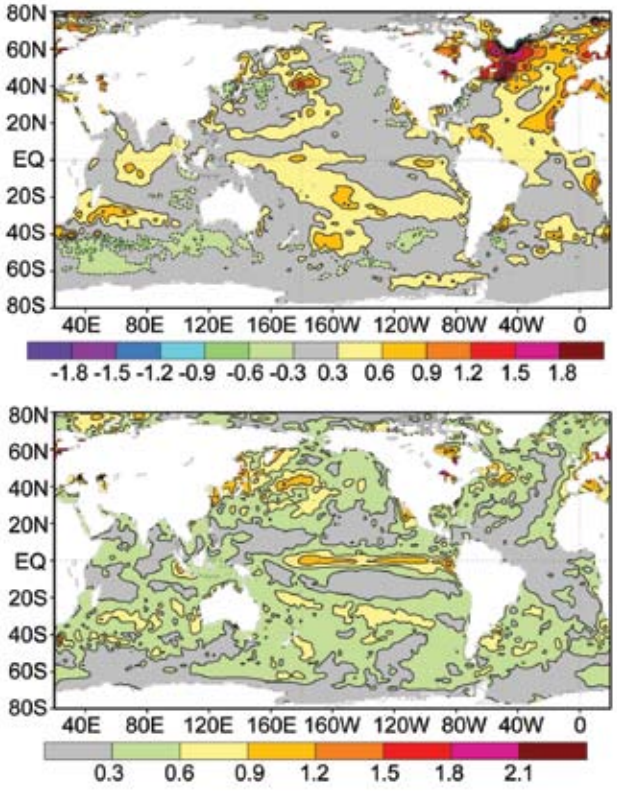

Fig. 3.1. Mean (top) and standard deviation (bottom) of monthly SST anomalies for 2006 on a 1° spatial grid. The anomalies are computed relative to a 1971–2000 base period. The contour interval is 0.3°C; the 0 contour is not shown. AVHRR satellite data are used.

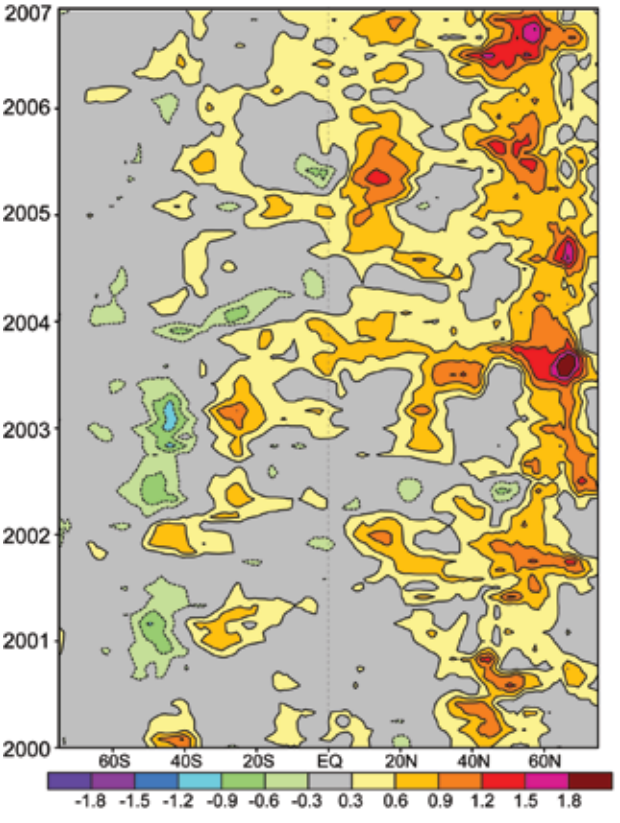

Fig. 3.2. Zonally averaged monthly SST anomalies for January 2000 through December 2006 for the Atlantic. The contour interval is 0.3°C; the zero contour is not shown. The anomalies are computed relative to a 1971–2000 base period.

central to such aspects of climate as El Niño (e.g., Zebiak 1989), the North Atlantic Oscillation (e.g., Curry and McCartney 2001), hurricane seasons (e.g., Emanuel 2005), and global change (e.g., Levitus et al. 2005; Hansen et al. 2005). Here we discuss an estimate of upper (0–750 m) OHCA estimated from a combination of in situ temperature profiles with satellite altimetry sea surface height data for the period of 1 January–31 December 2006 (Fig. 3.3), analyzed following Willis et al. (2004), but relative to a 1993–2006 baseline. Data from Argo floats with a recently detected systematic bias in reported pressure values have been removed from the estimates discussed here. Details of the fields analyzed here may change after more real-time data are subject to delayed-mode scientific quality control.

The 2006 combined OHCA map (Fig. 3.3) shows eddy and meander variability down to the 100-km mapping scales, as does, to a greater extent, the difference between the 2006 and 2005 combined OHCA maps (Fig. 3.4). There is a great deal of small-scale spatial variability in OHCA fields associated with the western boundary currents in every gyre, as well as the Antarctic Circumpolar Current. The difference in combined OHCA maps between 2006 and 2005 (Fig. 3.4) illustrates the large year-to-year variability in ocean heat storage, with changes reaching or exceeding the equivalent of an 80 W m^{-2} magnitude surface flux. Ocean advection likely plays a significant role in many of these changes.

Large-scale patterns are also evident in OHCA for 2006 (Fig. 3.3), and for its difference from 2005 (Fig. 3.4). One of the prominent patterns is along the equatorial Pacific, where there is a band of high heat content in 2006, which is also seen as a heat gain since 2005. This pattern is consistent with the onset of El Niño in 2006. There is also a band of high OHCA along 10°N from the western Pacific to about 160°W. In addition, there is a band of high OHCA that reaches from 150°E on the equator to at least 120°W and about 25°S.

The combined OHCA map for 2006 (Fig. 3.3) is high in the subpolar North Atlantic (except for seas just northeast of Iceland) and low in the subtropical North Atlantic. This pattern dynamically implies a decreased strength of the North Atlantic Current, and is probably related to decadal changes in the North Atlantic Oscillation Index (e.g., Curry and McCartney 2001). This climate index was lower in 2006 than during the baseline period; it has trended lower from 1993 to 2006.

In the equatorial Indian Ocean, OCHA is low in the east and high in the west (Fig. 3.3), with interannual variations (Fig. 3.4) apparently contributing to this pattern. The southern subtropics of the Indian Ocean are generally high in OCHA, but changes since 2005 (Fig. 3.4) do appear to be a dominant contributor to this pattern.

In 2006, OHCA is high in the Southern Oceans in a belt located north of the Antarctic Circumpolar Current (Fig. 3.3), especially east of New Zealand in the South Pacific and between 30° and 45°S in the South Atlantic, but less perceptible in the south Indian Ocean. This change has recently been studied on decadal time scales in the South Pacific (Roemmich et al. 2007) and appears to be related to changes in the wind stress field associated with an increase in the Antarctic Oscillation index. This index reached a peak in 1999, fell into a shallow valley in 2002, and has been near neutral since then. Consistent with this neutrality, there is relatively little large-scale trend of OHCA between 2005 and 2006 in this region

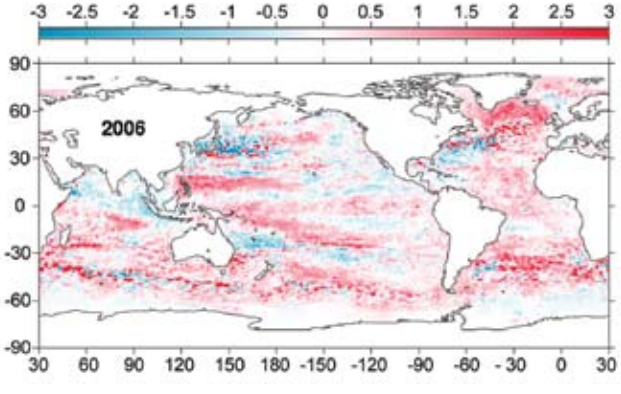

Fig. 3.3. Combined satellite altimeter and in situ ocean temperature data upper (0–750 m) ocean heat content anomaly OHCA (J m^{-2}) map for 2006.

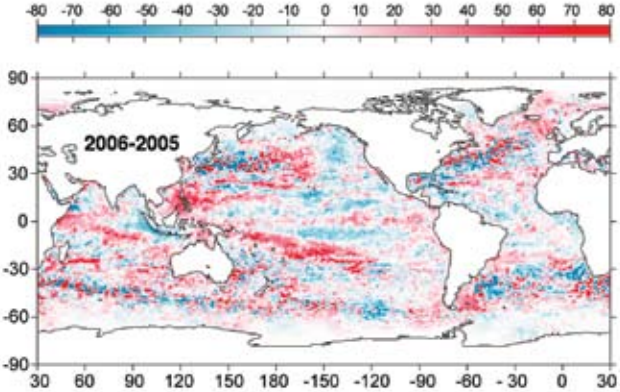

Fig. 3.4. The difference of 2006 and 2005 combined OHCA maps expressed as a local surface heat flux equivalent (W m^{-2}).

(Fig. 3.4), with smaller spatial scale changes of varying sign predominating in the subpolar regions of the Southern Hemisphere.

Finally, given the potential link between hurricane intensity and warm ocean waters (e.g., Emanuel 2005), we discuss tropical Atlantic patterns in OHCA. There was a record North Atlantic hurricane season in 2005 and a much weaker one in 2006 (see section 4). This change is consistent with decreases in OHCA from 2005 to 2006 in the Gulf of Mexico, in the Caribbean, and to a lesser extent around 10°N across much of the tropical North Atlantic (Fig. 3.4). This area had an increase in OHCA and hurricanes between 2004 and 2005 (Shein et al. 2006).

3) Global ocean heat fluxes—L. Yu and R. A. Weller

Latent heat (evaporation) and sensible heat fluxes are the primary mechanism by which the oceans release much of the absorbed solar energy back to the atmosphere. These ocean-to-atmosphere heat transfers are a cooling mechanism for the oceans but a source of heating for the atmosphere. The cooling and heating change the temperature gradients and energize the circulations in the ocean and atmosphere, which in turn affect air–sea temperature and humidity contrasts and modify the magnitudes of the ocean heat fluxes.

The estimates for the global LHF + SHF in 2006 (Fig. 3.5) were produced by the OAFlux project (Yu and Weller 2007) at the WHOI. The flux estimates are accurate within 8 W m^{-2}. On an annual mean basis, the largest absolute ocean heat losses occur over the regions associated with major WBCs and their extensions, the most noted of which are the Kuroshio off Japan, the Gulf Stream off the United States, and the Agulhas Current off the African coast. The magnitude of annual mean LHF + SHF in these regions exceeds 250 W m^{-2}, and is produced largely during the fall-to-winter seasons by strong winds and cold and dry air masses coming from the land. The secondary heat loss maximum (~180 W m^{-2}) is located over the broad subtropical southern Indian Ocean, where the large air–sea heat exchanges are sustained by the strong southeast trade winds during the boreal summer monsoon months (June–September).

Compared to the annual mean LHF + SHF in 2005 (Fig. 3.5), the heat fluxes in 2006 showed changes over all global basins, with the magnitude of the deviation within 50 W m^{-2}. Among all of the changes, two features in the tropical oceans are the most interesting. The first change is the increased LHF + SHF in the eastern and central equatorial Pacific Ocean concurrent with the development of a mild El Niño. In late 2006, SSTs were 2°–3°C above normal across much of the region. The increased evaporative heat loss is observed in regions of the El Niño warm SST anomalies. Variation of ocean heat fluxes in the tropical Pacific on ENSO time scales is a dominant interannual signal in the OAFlux multidecade time series (e.g., Yu and Weller 2007). The second feature is characterized by the east–west asymmetry in the 2005/06 difference anomalies in the tropical Indian Ocean. A positive IOD mode event occurred in 2006, with cold SST anomalies off the west coasts of Sumatra and Java and warm SST anomalies across the central and western parts of the basin. The IOD SST pattern is almost a mirror image of the El Niño SST in the Pacific. However, the changes in the flux patterns of these two basins did not mirror each other in 2006. The colder eastern Indian Ocean enhanced sea-to-air heat fluxes, while the warmer western Indian Ocean reduced the heat fluxes. This means that positive SST anomalies in the El Niño region correlated with positive heat flux anomalies, but positive SST anomalies in the Indian Ocean correlated with negative heat flux anomalies. The sign of the flux changes was opposite to the sign of the SST

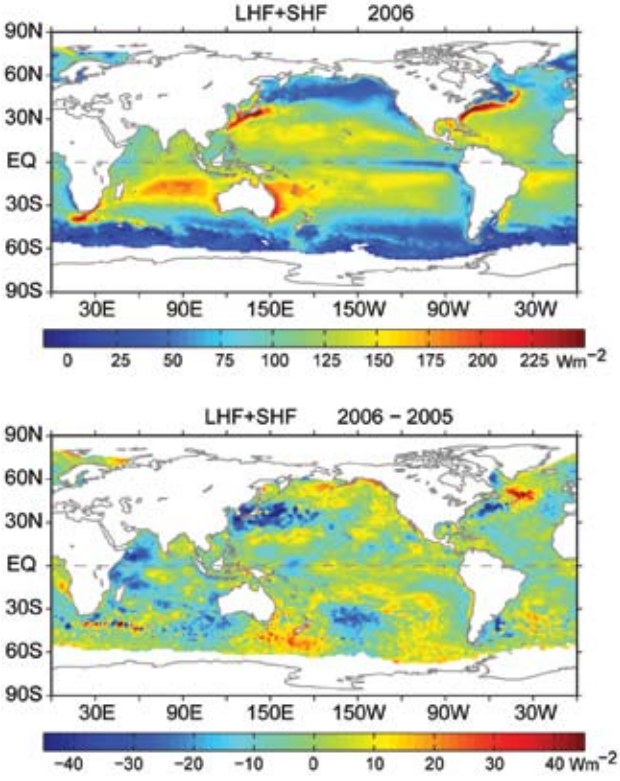

Fig. 3.5. (top) Annual mean latent plus sensible heat fluxes in 2006. The sign is defined as upward (downward) positive (negative). (bottom) Differences between the 2006 and 2005 annual mean latent plus sensible heat fluxes.

anomalies in the two basins, which suggested different feedback mechanisms were at work. Scientists are working to determine if the SST–flux relationship in the Pacific suggests a response of the atmosphere to the oceanic forcing, and if the SST–flux relationship in the Indian Ocean implies an atmospheric forcing for the ocean.

Outside of the Tropics, the influence of eddy-scale structures is evident in the 2-yr difference map. Nevertheless, the difference anomalies are most pronounced in the vicinity of the two WBCs, that is, the Kuroshio and the Gulf Stream, and their extensions. For the former, there were negative LHF + SHF anomalies over almost the entire region; while for the latter, there were negative flux anomalies south of the Gulf Stream extension and positive anomalies north of the current. A colder sea surface coupled to slightly weakened wind speed appears to be the cause of the reduced LHF + SHF in these regions. It may be worth noting that the SSTs in the Kuroshio and its extension are generally lower than normal during the ENSO warm phases (White and He 1986). The connection between lower SST and less oceanic heat loss is another indication of the response of the atmosphere to oceanic forcing.

The long-term context of the change in ocean heat fluxes in 2006 is shown in the plot of year-to-year variations of the globally averaged annual mean from 1958 to 2006 (Fig. 3.6). The 2006 mean of LHF + SHF was at a similar level to the 2005 mean. However, the two recent years are located at the high end of a long-term upward trend that started in 1977/78. Since then, LHF + SHF have increased by about 9 W m^{-2}, from a minimum at ~99 W m^{-2} in 1977 to a maximum at ~108 W m^{-2} in 2003. The magnitude of the variability is dominated primarily by LHF. SHF is about one order smaller than LHF, and the change in SHF is also small (less than 2 W m^{-2} over the entire 50-year analysis period). Nonetheless, the trend in SHF is very different from that in LHF: the downward trend in SHF lasted until the late 1980s, followed by a few abrupt jumps in the early 1990s. Since 2000, SHF has tended downward.

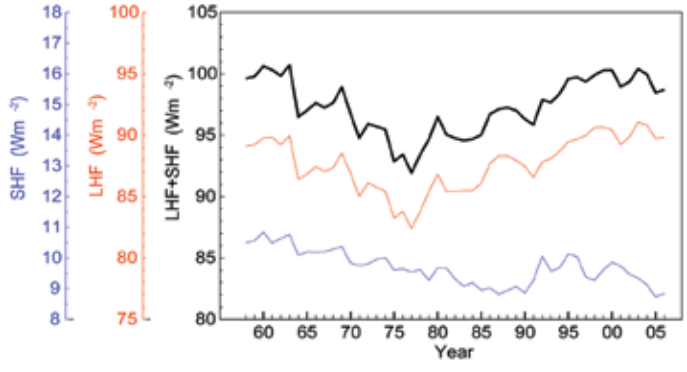

Fig. 3.6. Year-to-year variations of globally averaged annual mean latent plus sensible heat flux (black), latent heat flux (red), and sensible heat flux (blue).

c. *Sea surface salinity*—G. C. Johnson and J. M. Lyman

Ocean storage and transport of freshwater are intrinsic to many aspects of climate, including the global water cycle (e.g., Wijffels et al. 1992), El Niño (e.g., Maes et al. 2006), and global climate change (e.g., Held and Soden 2006). Regional studies of decadal freshwater variability are possible in well-sampled regions like the North Atlantic (e.g., Curry and Mauritzen 2005). In addition, zonal averages of long-term global trends of salinity in each ocean basin have been analyzed (Boyer et al. 2005). In situ ocean salinity data have traditionally been too sparse and their reporting too delayed for an annual global perspective of ocean freshwater and its complement, salinity. However, the rapidly maturing Argo array of profiling floats (Roemmich et al. 2004) is remedying this situation. Argo data are used here to present annual average SSS analyses for 2006 and 2005, the first years with near-global Argo coverage. Remote sensing of SSS by satellite is planned for 2009 (information online at http://aquarius.nasa.gov/).

Here the shallowest near-surface (< 25 m) salinity data flagged as good from each available Argo profile for the years in question were subjected to a statistical check to discard outliers. The remaining data were then cast as differences from a climatological mean surface salinity field from the WOA based on historical data reported through 2001 (WOA 2001; Boyer et al. 2002). The resulting anomalies were then mapped, essentially assuming a Gaussian covariance function with 6° latitude and longitude decorrelation length scales and a signal-to-noise variance ratio of 2.2 (Bretherton et al. 1976).[1]

SSS patterns are fairly well correlated with surface freshwater flux, the sum of evaporation, precipitation, and river runoff (e.g., Behringer et al. 1998). In each ocean basin, subtropical salinity maxima centered near 20° or 25° in

[1] While some delayed-mode scientific controlled (final) Argo data are available for the 2005–06 time period, many real-time (preliminary) Argo data were used in both years. The real-time estimates of SSS made here could change after all the data have been subject to careful scientific quality control.

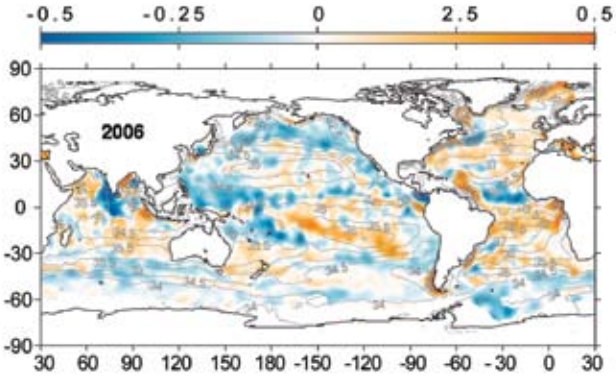

Fig. 3.7. Map of the 2006 annual surface salinity anomaly estimated from Argo data (colors in PSS-78) with respect to a climatological salinity field from WOA 2001 (gray contours at 0.5 PSS-78 intervals). White areas are either neutral with respect to salinity anomaly or are too data poor to map. While salinity is often reported in practical salinity units it is actually a dimensionless quantity reported on the PSS-78.

latitude are signatures of the predominance of evaporation over precipitation. Conversely, in most regions where climatological surface salinities are relatively fresh, precipitation generally dominates over evaporation. The 2006 anomalies from WOA 2001 (Fig. 3.7) reveal some large-scale patterns. In 2006 the regions around the climatological salinity maxima are mostly salty with respect to WOA 2001. In many of the climatologically fresh regions, 2006 values appear fresher than those of WOA 2001, including most of the ACC near 50°S, the subpolar gyre of the North Pacific, and the ITCZ over the Atlantic and Pacific Oceans (including the SPCZ).

These patterns may suggest an increase in the hydrological cycle (more evaporation in drier locations, and more precipitation in rainy areas), as depicted in simulations of global warming. These simulations do suggest that this signal might be discernible during the last two decades of the twentieth century (Held and Soden 2006). Any increase in the hydrological cycle would certainly result in changes of local SSS values, but not alter the global average salinity by itself. Most of these patterns observed in 2006 (Fig. 3.7) are not reflected in the 2005–06 differences (Fig. 3.8), suggesting that these anomalies have evolved over longer-than-interannual time scales; although, without global coverage prior to 2005, it is difficult to determine the time scale. However, there are alternate explanations. It is possible that the climatology, being based on relatively sparse data distributions in many parts of the oceans, may tend to underestimate regional extrema that the well-sampled Argo array can better resolve. Also, some of these patterns might be explained by interannual shifts in ocean features such as the ACC or atmospheric features such as the ITCZ.

For example, the subpolar North Atlantic and Nordic Seas are relatively salty, both in 2006 (Fig. 3.7) and in 2005 (not shown), with relatively small changes between these two years (Fig. 3.8). This salty anomaly is inconsistent with an increase in the strength of the hydrological cycle. However, the pattern may have less to do with local evaporation and precipitation fields and more with northward spread of saltier waters from the south. The salty anomaly in this region is consistent with a stronger influence of subtropical gyre waters in the northeastern North Atlantic in recent years and a reduced extent for the subpolar gyre (Hátún et al. 2005).

There are evidently some rather large anomalies in the equatorial and North Indian Ocean. The Bay of Bengal and much of the Arabian Sea appear to be anomalously salty, while the ocean to the south and east of India appears to be fresh (Fig. 3.7). The changes appear to be interannual, as reflected in the large changes in anomaly between 2005 and 2006 in this region (Fig. 3.8).

One last feature of interest in the 2006 salinity field is the anomalously salty water located in the region of the fresh Amazon River plume (Fig. 3.7). The influence of this plume would normally be apparent in the relatively fresh conditions to the north and west of the mouth of the Amazon River (near the equator) that reach as far north as Puerto Rico. The salty anomaly in this region in 2006 may be explained by the reduced freshwater flow from the Amazon into the ocean during a record drought in the Amazon River basin in 2005 (Shein et al. 2006), with some time delay for hydrological and oceanic processes. The change in salinity between 2005 and 2006 (Fig. 3.8) shows that this salty anomaly is limited to 2006.

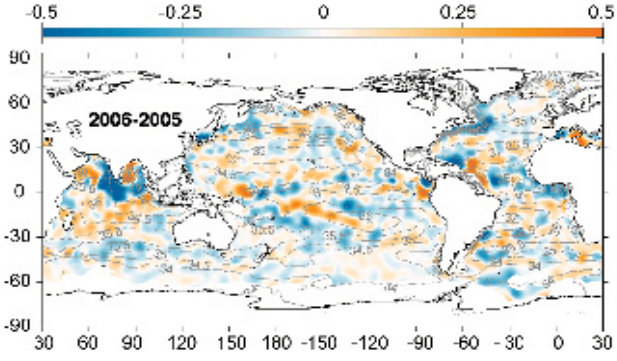

Fig. 3.8. The difference of 2006 and 2005 surface salinity maps estimated from Argo data (colors in PSS-78 yr^{-1}). Other details follow Fig. 3.7.

d. Circulation

1) Surface current observations—R. Lumpkin and G. Goni

Near-surface currents are measured in situ by satellite-tracked drifting buoys and acoustic point-measuring meters on ATLAS moorings.[2] In September 2005, the drifter array reached its target goal of 1250 drifters worldwide, becoming the first fully realized component of the GCOS-92. During 2006, surface currents were well sampled except in the far northern Pacific, in the southwest Pacific between 20° and 40°S, from 150°E to the date line, for the Arabian Basin of the Indian Ocean, and for the extreme Southern Ocean south of 55°S.

Weekly maps of absolute surface currents and geostrophic current anomalies for 2006 were calculated from a synthesis of in situ observations, near-real-time AVISO data gridded altimetry, and NCEP operational winds (Niiler et al. 2003). Anomalies are defined with respect to the 1993–98 mean.

In 2006, the most dramatic surface current anomalies were associated with the development of El Niño conditions late in the year in the Pacific Ocean basin. Anomalies elsewhere in the World Ocean were caused either by energetic mesoscale (60–90-day period) variations or by displacements of currents from their typical positions, or were associated with the seasonal reversals of currents in the Tropics.

(i) Pacific Ocean

Annual mean anomalies (Fig. 3.9) were most prominently organized in a coherent pattern in the western tropical Pacific Ocean, associated with the 2006 El Niño. Seasonal mean anomalies (Fig. 3.10) show a typical seasonal reversal of the equatorial surface current from January through June. During July, eastward anomalies began developing in the eastern (145°–170°E) equatorial Pacific (Fig. 3.11). By August, these anomalies had reached 70 cm s^{-1} at 160°E to the date line. In September, eastward anomalies of ~40 cm s^{-1} were seen at 120°–140°W. The largest eastward anomalies of 50 cm s^{-1} were seen in October at 160°E to the date line. These anomalies also propagated eastward while weakening to +25 cm s^{-1} in November. Anomalies in December were small.

(ii) Indian Ocean

The tropical Indian basin exhibited a band of anomalously eastward flow along 25°–30°S, immediately south of westward anomalies. This is the band where the westward SEC encounters Madagascar and is deflected southwestward to join the Agulhas Current system flowing southward against Africa's west coast. The anomaly pattern suggests that the SEC was displaced to the north of its climatological position. Seasonally averaged anomalies (not shown) were associated with monsoon-driven changes in the tropical basin and the complex pattern of mesoscale anomalies in the Agulhas Return Current. The eastward equatorial jet was prominent in April–June, but not in October–December.

(iii) Atlantic Ocean

The seasonal reversal of western tropical Atlantic Ocean currents (cf. Lumpkin and Garzoli 2005) was prominent in 2006. Anomalously strong westward anomalies were seen on the equator in July–September, reversing to eastward anomalies in Octo-

[2] Drifter data are distributed by NOAA/AOML's Global Drifter Program at the Drifter Data Assembly Center Web site (www.aoml.noaa.gov/phod/dac/dacdata.html). Moored current meter data are distributed by NOAA/PMEL's Tropical Atmosphere–Ocean Project at www.pmel.noaa.gov/tao. Altimetric time series of transports may be viewed at www. aoml.noaa.gov/phod/satprod. NCEP data are provided by the NOAA–CIRES Climate Diagnostics Center, Boulder, Colorado (www.cdc.noaa.gov). AVISO altimetry is produced by the CLS Space Oceanography Division as part of the Environmental and Climate EU ENACT project and with support of CNES.

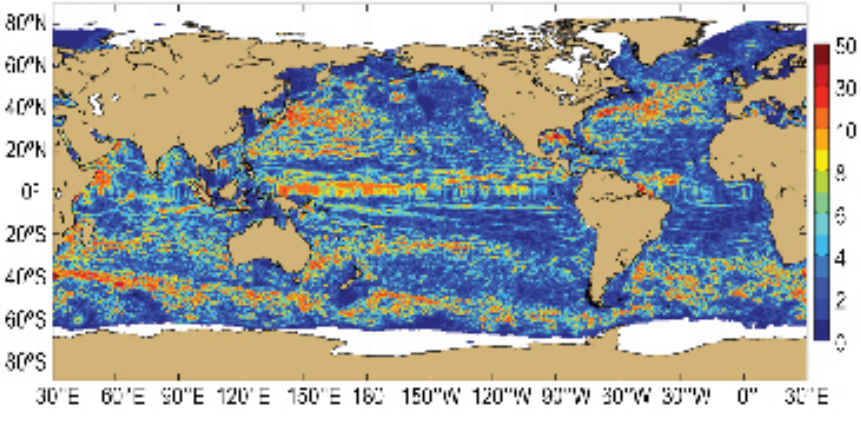

Fig. 3.9. Amplitude (cm s^{-1}) of 2006 averaged surface current anomalies, with respect to the 1993–98 mean.

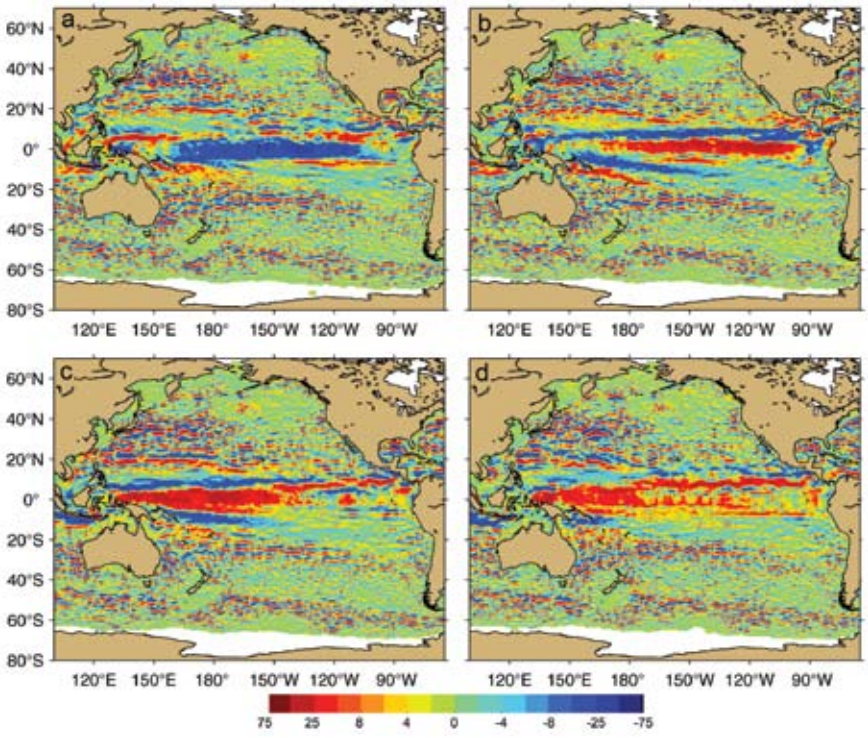

Fig. 3.10. Pacific seasonal anomalies of zonal current (positive = eastward) during (a) January–March, (b) April–June, (c) July–September, and (d) October–December 2006.

ber–December. This reversal is typical, but was more energetic and dramatic in 2006. Anomalies elsewhere were associated with intense mesoscale features in the Gulf Stream, Brazil/Malvinas Confluence off the Brazilian coast, and the Agulhas retroflection west of the southern tip of Africa. Averaged over 2006, the Gulf Stream axis was close to its climatological position. Late in 2006, the Gulf Stream developed a dramatic pattern of alternating meanders at 50°–65°W.

Satellite altimetry observations indicate that the Agulhas Current, which runs southward against Africa's southeast coast, was somewhat larger than average during 2006. This current can serve to connect the Indian and Atlantic Oceans by transferring salty, tropical Indian water into the South Atlantic via Agulhas rings shed from the current. However, the number of rings shed in 2006, as revealed by altimetry, was lower than average. Thus, unless the few rings that were shed were unusually deep, the South Atlantic Ocean may reveal fresh anomalies in Argo-derived salinity maps for early 2007.

The NBC runs northward along the Brazilian coast, carrying South Atlantic water past the equator before it abruptly leaves the coast and flows eastward across the Atlantic. Rings shed by the NBC continue northwestward, and carry a large fraction of the upper-water exchange from the South Atlantic to the North Atlantic. This pathway is thus a critical part of the upper limb of the MOC in the Atlantic.

The space–time diagram of sea height residual (sea height anomaly with the annual cycle removed) along the pathway of NBC rings (not shown) reveals that five rings are shed by the NBC during 2006, which is approximately the historical mean. However, most of these rings did not enter the Caribbean Sea. The time series of geostrophic transport of the Yucatan Straits (not shown), connecting the Caribbean Sea to the Gulf of Mexico, indicates that the transport decreased during 2006. This is significant, because the flow through the Yucatan Straits feeds the Loop Current–Florida Current–Gulf Stream system. Consistently, the Florida Current transport, measured by an undersea cable running from South Florida to the Bahamas, decreased slightly from its historical average of 30–32 million tons s^{-1} in mid-October to around 28 million tons s^{-1} by the end of the year. Such anomalies are common in the record.

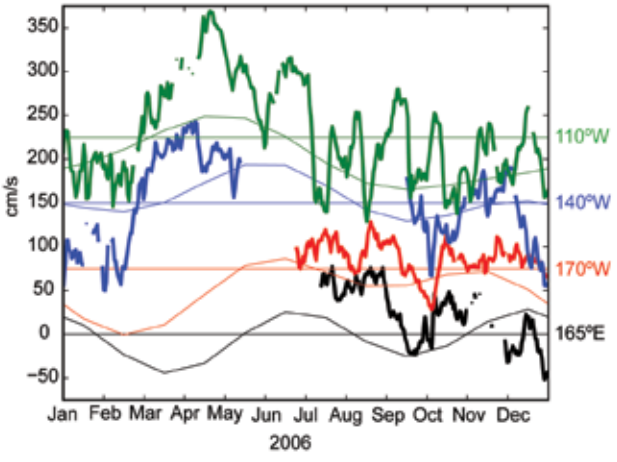

Fig. 3.11. Near-surface zonal current anomalies (daily averages) measured at equatorial TAO moorings. Time series east of the date line have been displaced vertically; the zero line for each is indicated by a horizontal line. Seasonal climatology at each site is indicated by thin curves.

2) The Meridional Overturning Circulation and oceanic heat transport—M. O. Baringer and C. S. Meinen

The component of the ocean circulation associated most with long-time-scale variability in heat redistribution is the MOC, sometimes referred to as the "thermohaline circulation." The MOC is a global circulation cell wherein surface waters in the high latitudes are cooled, thereby becoming denser; this dense water sinks and flows toward the equatorial regions. In tropical and subtropical regions around the world these waters eventually mix with other waters, becoming less dense, and they return to the sea surface to ultimately flow toward the higher latitudes and complete the cell. This circulation simultaneously transfers a significant amount of heat to the higher latitudes. The primary locations where deep convection occurs are in the northern North Atlantic and in the subpolar ocean around Antarctica, while the upwelling of new surface waters is spread broadly around the globe.

The strengths of the overturning circulations in different basins are directly related to the strength of the heat transport; warm water flowing north in the upper layers and returning southward as cold water at depth represents a net poleward heat transport in the Northern Hemisphere. There are several available estimates of the averaged global mass and heat transport based on inverse model calculations (Lumpkin and Speer 2007; Ganachaud and Wunsch 2003; Talley 2003;). Historical estimates of the state of the MOC have come from either cross-basin hydrographic sections or specific point measurements of the water property changes in the deep ocean. These water property measurements have been used to infer the state of the MOC using a variety of analytical techniques. Currently, observing systems capable of quantifying changes in the complete MOC are at fledgling stages that at best observe only one component (e.g., a specific current or ocean layer) of the MOC at discrete locations.

The MOC is generally thought of as a basin-wide phenomenon, however at 26°N in the Atlantic the bulk of the warm upper limb of the MOC is thought to be carried in the Florida Current through the Straits of Florida (with a smaller contribution being carried by the Antilles Current east of the Bahamas), while the majority of the cold lower limb is believe to be carried to the south in the DWBC just east of the Bahamas. Fluctuations in the Florida Current show a clear negative correlation with the atmospheric phenomenon known as the NAO; however, while the NAO has been tending to decrease over the past 20 years, the Florida Current transport shows no corresponding long-term trend through 2006 (Fig. 3.12). The annual mean transport observed in 2006 (31.3 Sv[3]) falls within the lowest quartile of historical annual mean transports from the cable, however this transport is still well within one standard deviation from the long-term mean of 32.1 Sv. Given the statistical standard error of the mean of 1 Sv for the year, 2006 cannot be termed as an unusual year in terms of the Florida Current transport. Additional information can be found in Baringer and Meinen (2006).

In a recent article, Bryden et al. (2005) postulate a 30% reduction in the MOC transport between the 1950s and the present day. However, that analysis is based on a very limited dataset (essentially five "snapshot" hydrographic sections). In contrast, a comparison of moored observations near the Southeast Newfoundland Ridge in the early 1990s and early 2000s finds no trend in the DWBC transport (Schott et al. 2004), and a subsequent study at 26°N comparing transports from moored instruments in the late 1980s and 2004/05 finds no indication of a systematic trend either (Meinen et al. 2006). Furthermore, the latter study finds evidence of significant baroclinic and barotropic variability at time scales that could be aliased by "snapshot" hydrographic sections such as those used in Bryden et al. (2005).

Other recent work using cross-basin hydrographic sections along 48°N in the Atlantic suggest con-

[3] Sv is a Sverdrup or 10^6 m^3 s^{-1}, a unit commonly used for ocean volume transports.

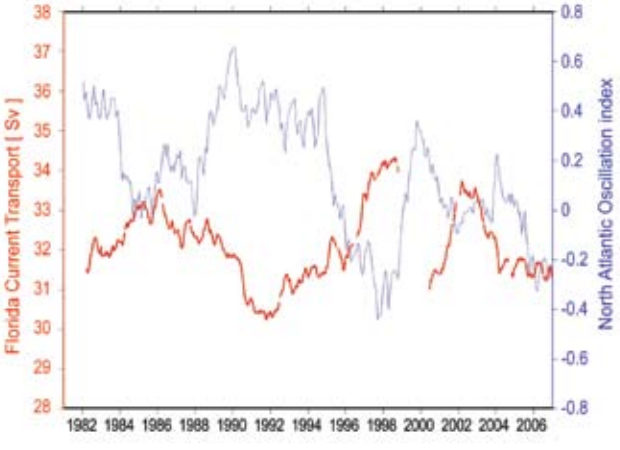

Fig. 3.12. Florida Current transport (red solid) as measured by the NOAA-funded submarine cable across the Florida Straits, along with the North Atlantic Oscillation index produced by the NOAA National Centers for Environmental Prediction (blue dashed).

flicting conclusions relative to the state of the thermohaline circulation. In particular, Koltermann et al. (1999) show large variability of the MOC that, they conclude, is related to the strength of Labrador Sea Water production, with larger (smaller) MOC transport corresponding to less (more) Labrador Sea Water export. More recently, these data have been reanalyzed to formally test the hypothesis that the MOC circulation is steady. Lumpkin et al. (2007) find that a steady MOC over the same time period could not be ruled out based on the uncertainty in determining the barotropic circulation.

Clearly, additional work needs to be done to understand the full range of time scales associated with MOC variability and the improvement of error estimates attached to these estimates. The programs in place in 2006 are an excellent first step toward the development of an integrated measurement system. However, much work remains to fully monitor the Atlantic MOC system, as well as the global overturning circulation system.

e. *Sea level*—M. A. Merrifield, S. Gill, G. T. Mitchum, and P. L. Woodworth

Global sea level variability during 2006 is summarized using measurements from the complementary satellite altimeter and tide gauge observing systems. Here we use SLA data (1993–99 base) from the multimission, 1/4° gridded product available from the French Aviso program (online at www.aviso.ceanobs.com/). Because 2006 satellite orbit corrections are still being applied, the 2006 SLA analysis period is taken as October 2005 through September 2006. We also used RSL data (1993–99 base) from The GLOSS (Woodworth et al. 2003), a network of nearly 300 coastal tide gauges. The SLA is used to assess global mean sea level change and RSL is used to summarize coastal sea level variability for 2006.[4]

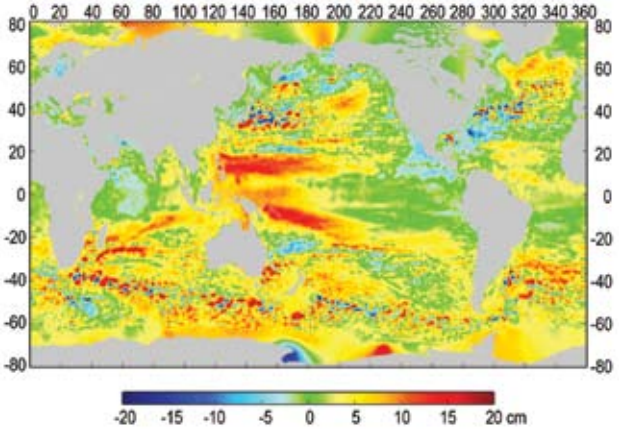

Fig. 3.13. Annual average SLA for 1 Oct 2005–30 Sep 2006.

Annual mean SLA in 2006 was above the 1993–99 baseline average for nearly 80% of the ocean surface (Fig. 3.13). Bands of high SLA (10–20 cm) occurred in the western tropical Pacific east of the Philippines, extending southeastward from the Solomon Islands along the South Pacific convergence zone. These bands also were the areas of the highest positive increase relative to the 2005 annual mean. A notable pattern in the eastern equatorial Pacific that was most evident after the averaging period used to construct Fig. 3.13 was a weak El Niño event with ~10 cm positive sea level anomalies in December 2006.

The spatially weighted, global mean SLA for 2006 was the highest annual mean (computed from October through September of each year) since the beginning of the altimeter record in 1993. Global mean SLA was 6 mm higher in 2006 than 2005, an increase larger than the global sea level rise rate of 2.8 ± 0.4 mm yr^{-1} estimated over altimeter data from 1993 to 2003 (Leuliette et al. 2004). The increasing global mean level is attributed primarily to large SLA increases south of 20°N, especially between 40° and 30°S and near the equator (Fig. 3.14a), and in longitude bands encompassing the Indo-Pacific (100°–240°E) and the Atlantic (310°E–360°) (Fig. 3.14b). Detailed global maps of SLA trends are available online at http://sealevel.colorado.edu/.

Changes in relative sea level, including vertical land motion contributions, are examined using available RSL data from 2006 (Fig. 3.15). This provides an assessment of sea level change as experienced at the coast, but is not a measure of global mean sea level change, which is best addressed using the SLA dataset. The annual RSL average for 2006 was the highest over the collective record, which begins in at least 1980 for the majority of stations, and in the early twentieth century for ~10% of stations. The station mean RSL increased by 2.9 mm in 2006 from 2005, about one-half the global mean SLA

[4] The altimeter products were produced by Ssalto/Duacs and distributed by Aviso, with support from CNES (www.aviso.oceanobs.com). The Aviso dataset used is listed as the Gridded Sea Level Anomalies DT-MSLA "Ref," multimission product. Tide gauge data were obtained from the University of Hawaii Sea Level Center (http://uhslc.soest.hawaii.edu). SLA is corrected for atmospheric pressure, the RSL time series is not.

increase over the same period. The station mean RSL rise rate is 2.3 mm yr^{-1} since 1993, the time span of the SLA data, and 1.9 mm yr^{-1} since 1975.

Extreme sea levels during 2006, associated with storms and other nontidal variability, is characterized by the average of the 5% largest daily averaged RSL values at each station. The highest extreme values occurred at high-latitude stations resulting from winter storms, with sporadic high values at low-latitude stations presumably resulting from isolated storm events (Fig. 3.15a). To determine how anomalous the extremes were during 2006, the percentage of years at each station with extreme values less than 2006 is depicted in Fig. 3.15b. For the majority of stations, the 2006 extremes were in the 90th percentile or higher (e.g., Europe, the east coast of North America, the South Pacific). The year 2006 was an anomalously high year for extreme sea levels in part because of rising sea levels. If the percentiles are computed after removing mean sea level trends at each station, 2006 is seen as a less anomalous year in the South Pacific, although values around North America and North Europe remain high (Fig. 3.15c). The increase in the 2006 percentiles for some Alaskan and Canadian stations (Fig. 3.15c) is due to the correction for negative rates of RSL change.

f. Global ocean carbon cycle—C. L. Sabine, R. A. Feely, and R. Wanninkhof

1) Air–sea carbon fluxes

Seasonal-to-interannual variability in the ocean

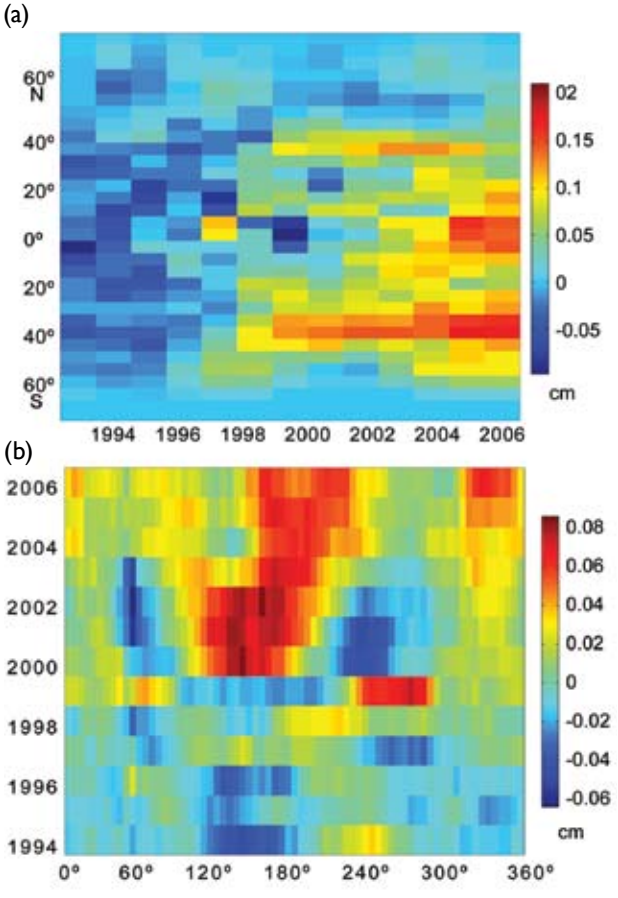

Fig. 3.14. (a) Time vs latitude plot of annual mean SLA averaged over longitude and weighted by the percentage of total ocean surface area covered. (b) Longitude vs time plot of annual mean sea level averaged over latitude and weighted by the percentage of total ocean surface area covered.

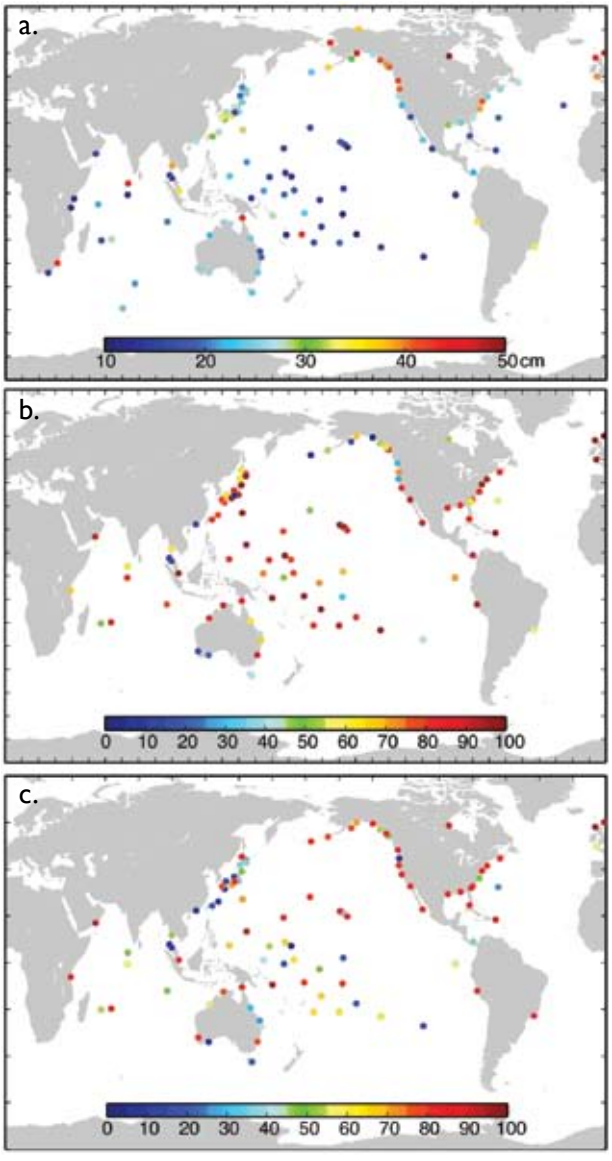

Fig. 3.15. (a) Average of the highest 5% of daily sea level values during 2006. (b) Percentage of years at each station with extreme values less than in 2006. (c) Same as (b), but with the trend of mean sea level first removed from each time series.

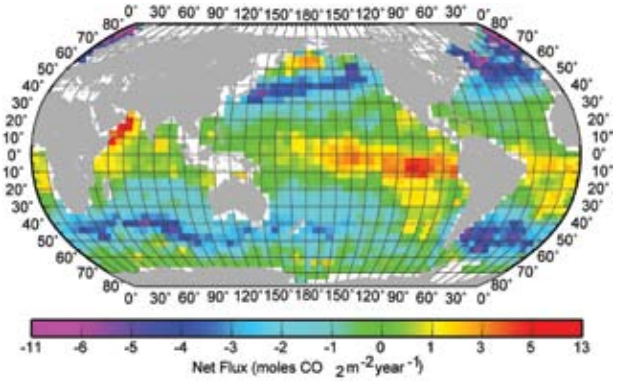

FIG. 3.16. Mean annual net air–sea flux for CO_2 (moles CO_2 m^{-2} yr^{-1}) for the reference year 1995. Red–yellow areas indicate that the ocean is a source for atmospheric CO_2, and blue–purple areas indicate that the ocean is a CO_2 sink. From Takahashi et al. (2002).

CO_2 sink is being investigated by studying the CO_2 flux across the air–sea interface. Carbon dioxide flux is calculated from measurements of surface water and atmospheric pCO_2, together with wind speed. The climatological monthly distribution of pCO_2 in global surface water has been calculated with a spatial resolution of 4° × 5° (Takahashi et al. 2002). Fewer than 30% of the monthly pixels have direct observations. In general, the tropical regions are a net source of CO_2 to the atmosphere and the high latitudes are a net sink for CO_2 (Fig. 3.16). The published value for the net air–sea flux indicates a net ocean uptake of 2.2 Pg C for the reference year of 1995, but this estimate was later corrected for a systematic error in the wind speeds to give a net global ocean uptake of 1.5 Pg C for the reference year of 1995 (Sabine et al. 2004a). The contemporary CO_2 uptake of 1.5 Pg C yr^{-1} combined with the estimated preindustrial ocean source of 0.6 Pg C yr^{-1} implies an anthropogenic CO_2 uptake estimate (1.5 + 0.6 = 2.1 Pg C yr^{-1}) that is consistent with other independent estimates (Sabine et al. 2004a).

The CO_2 climatology has been used extensively as a baseline for placing regional flux estimates into a global context and as a constraint for global biogeochemistry and inverse models. However, developing seasonal-to-annual estimates of net air–sea CO_2 fluxes to evaluate the changing role of the ocean in the global carbon cycle resulting from climate change remains a formidable task. The large spatial and temporal variability in surface water pCO_2 still requires interpolation approaches to determine a meaningful global flux estimate or "flux map." Making flux maps directly from observations representing shorter time frames, however, will require a continued expansion of the observing network.

As a first step for assessing the interannual variability in air–sea CO_2 fluxes, we have taken the empirical approach of Lee et al. (1998) and Park et al. (2006) together with global monthly estimates of SST and a high-resolution wind speed assimilation product (online at http://podaac-www.jpl.nasa.gov/products/product079.html) to develop monthly estimates of global air–sea CO_2 flux between 1995 and 2005. To execute the scheme, surface water pCO_2–SST relationships were determined for each 4° × 5° pixel from least squares linear fits of the monthly climatological pCO_2 (Takahashi et al. 2002) and SST values for the following three periods: January–April, May–August, and September–December. In much of the world's ocean, except in the South Indian and Southern Oceans, the correlations between pCO_2 and SST are quite robust ($r^2 = 0.70 \pm 0.3$, number of pixels = 1314). These relationships are then applied to the interannual SST anomalies relative to 1995 to evaluate the change in pCO_2 for each pixel relative to the pCO_2 climatology. For the equatorial Pacific Ocean, one of the best-studied regions for seasonal and interannual CO_2 flux variability (e.g., Chavez et al. 1999; Cosca et al. 2003; Feely et al. 1995, 2006), empirical relationships between surface water pCO_2 and SST, rather than climatological values, are used to estimate pCO_2. Here we use the formulations of Cosca et al. (2003) to estimate pCO_2 for the equatorial Pacific between 5°N and 5°S. The air–sea flux is then calculated for each 4° × 5° pixel using the derived surface water pCO_2 estimates; the global atmospheric CO_2 mole fraction obtained from NOAA's Environmental Science and Research Laboratory (GLOBALVIEW-CO2 2006), converted to pCO_2 using the climatological SLP; and the wind speed gas exchange parameterization of Wanninkhof (1992). Validation of the approach at the few time series sites available shows good correspondence in the sign of the year-to-year changes between observations and this empirical approach, and an agreement in magnitude of better than 40%.

Figure 3.17 shows the interannual variability in the net annual air–sea CO_2 gas exchange from 1995 to 2005 relative to the 10-yr mean. The period from 1995 to 1998 was a period of generally negative anomalies indicating increased uptake by the oceans. The effect of the 1997/98 El Niño with decreased outgassing in the equatorial Pacific, which translates into net increased oceanic uptake, is clearly apparent (Feely et al. 2006). This is followed by three years of reduced uptake. The 2005 uptake appears to be very close to that of the 10-yr average. Overall, the implied

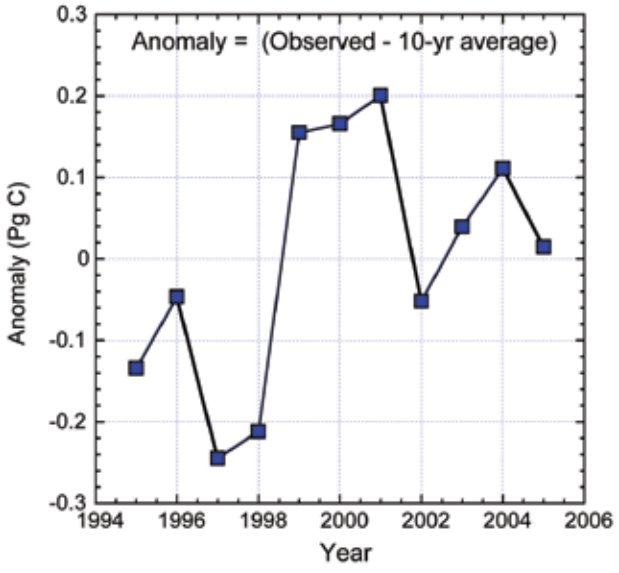

Fig. 3.17. Interannual variability in the net annual global air–sea CO_2 gas exchange from 1995 to 2005 relative to the 10-yr mean. Negative values indicate increased ocean uptake.

interannual variability of the ocean uptake is about 10% of the climatological value, consistent with previous ocean model–based estimates, including Park et al. (2006).

There are significant uncertainties in the seasonal flux map calculations based on several factors, including the assumptions that go into the fits, the quality of the empirical fits, uncertainties in the reanalysis products, and uncertainties in the wind speed relationship for gas exchange. This approach does not fully account for the biological effects on surface water pCO_2. Despite these shortcomings, these first estimates of interannual variability provide a useful tool for assessing the changing role of the ocean in global climate change and for comparison with models. Extension of the global surface ocean CO_2 network will facilitate the development of improved regional algorithms that will lead to more accurate flux maps.

2) Subsurface carbon inventory

An analysis of approximately 73,000 carbon measurements from 95 research cruises run as part of the WOCE and the JGOFS in the 1990s has provided the first global assessment of DIC distributions with sufficient accuracy and coverage to evaluate the change in ocean carbon resulting from the accumulation of anthropogenic CO_2 (Feely et al. 2001; Wallace 2001). Using these measurements, Sabine et al. (2004b) estimated that the ocean accumulated approximately 118 Pg C between 1800 and 1994 accounting for 48% of the CO_2 released from burning fossil fuels over this same time period (Fig. 3.18). The highest column inventories are observed in the North Atlantic and in a band around the Southern Hemisphere because these are regions where surface waters are sinking and moving anthropogenic CO_2 into the ocean interior (Fig. 3.18).

Although the WOCE/JGOFS data were used to determine the total accumulation of carbon in the ocean since preindustrial times, this one time global survey could not provide information on how ocean carbon inventories have evolved over time or how the storage has varied geographically over different time periods. To elucidate decadal variability and temporal evolution, the U.S. CLIVAR/CO2 Repeat Hydrography Program has identified 19 hydrographic sections distributed around the global ocean that will be reoccupied approximately every 10 years. The program started in 2003 with three cruises in the North Atlantic that were repeats of select WOCE/JGOFS cruises. Each year, one to three cruises are run in different locations with a goal of completing the first global resurvey by 2012.

The repeat hydrography strategy presents at least two major challenges for interpreting the measurements. First, it will take about a decade to survey enough of the oceans to draw robust inferences about the global patterns of decadal variations in the oceanic anthropogenic CO_2 sink. Second, some of the assumptions (e.g., steady-state circulation and biology) that appeared to be reasonable for the Sabine et al. (2004b) 200-year inventory assessment do not hold true for shorter time scales. New techniques must be developed for isolating the anthropogenic

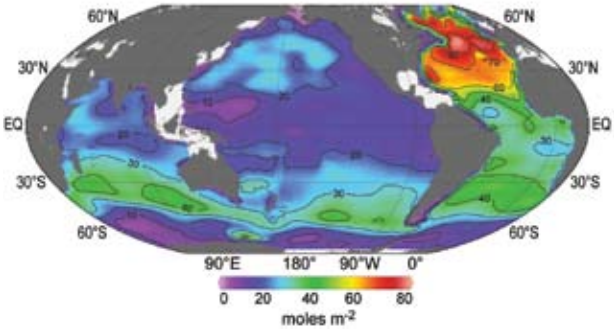

Fig. 3.18. Column inventory of anthropogenic CO_2 (mol m^{-2}) that has accumulated in the ocean between 1800 and 1994. High inventories are associated with deep water formation in the North Atlantic and intermediate and mode water formation between 30° and 50°S (Sabine et al. 2004b).

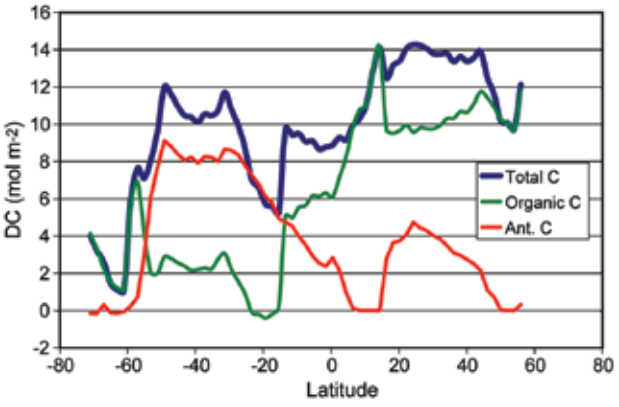

Fig. 3.19. Column inventories of the change in total DIC resulting from variations in the apparent decomposition rate of organic matter, and the change in DIC from the accumulation of anthropogenic CO_2 as a function of latitude along 152°W between 1991 and 2006.

signal from the natural variations in ocean circulation and biological particle decomposition rates that affect the interior carbon distributions on interannual-to-decadal time scales. Indeed, natural ocean variations can be the same order of magnitude as the anthropogenic changes and can either mask or enhance the anthropogenic signal.

Ocean carbon changes have been evaluated for ocean cruises that have reoccupied a Pacific north–south section along 152°W from Antarctica to Alaska in 2005 and 2006, approximately 15 years after the WOCE/JGOFS cruises. The total DIC column inventory changes along the section ranged from less than 2 mol C m^{-2} in the high-latitude Southern Ocean to greater than 14 mol C m^{-2} in the North Pacific (Fig. 3.19). This total DIC change, however, reflects both the uptake of anthropogenic CO_2 from the atmosphere and carbon changes resulting from natural variations in ocean physics and biogeochemistry. Separating these two components using newly developed methodologies reveals that in the North Pacific, the natural variations account for up to 83% of the total DIC change, leaving a rather modest anthropogenic CO_2 component (Fig. 3.19).

A full global assessment of ocean DIC changes cannot be made until the resurvey of the oceans is completed in the next few years. However, each updated ocean section provides incremental insight into how carbon uptake rates are evolving spatially and temporally. Table 3.1, updated in this report to reflect the 2005/06 Pacific cruises, summarizes the current best estimates of anthropogenic CO_2 accumulation along representative north–south cruise tracks in the Atlantic and Pacific Oceans. The North Atlantic shows the largest increase, consistent with the long-term accumulation of Sabine et al. (2004b), illustrating the importance of North Atlantic Deep Water formation as a mechanism for transporting anthropogenic CO_2 into the ocean interior. The formation of mode and intermediate waters in the Southern Hemisphere also contributes to the substantial DIC increases in the South Atlantic and South Pacific. The North Pacific shows a relatively modest increase because of the lack of deep water formation and restricted intermediate water formation in that region. The Indian Ocean is being surveyed in 2007/08, so accumulation rates are not yet available.

To place these regional measurements in a global perspective, indirect approaches for estimating the current ocean storage of anthropogenic CO_2 suggest a global ocean uptake of approximately 2.2 Pg C yr^{-1} (e.g., Bopp et al. 2002; McNeil et al. 2003; Matsumoto et al. 2004). If this carbon were distributed evenly over the entire global ocean area (335.2×10^9 km^2), it would imply an average column inventory increase of ~0.55 mol C m^{-2} yr^{-1}. The cruises completed thus far in the Atlantic and Pacific Oceans tend to bracket this average and suggest that the current patterns of ocean carbon storage are similar to the patterns observed in the long-term accumulation (Fig. 3.18). As additional cruises in the Atlantic and Pacific Oceans are evaluated, improved uptake estimates that consider the spatial variability within a basin will be generated.

g. Global ocean color and phytoplankton—M. M. Gierach and B. Subrahmanyam

Ocean color is a measure of chlorophyll-a (a pigment within phytoplankton) at the ocean surface and is considered an indicator of phytoplankton biomass.

Table 3.1. Estimates of ocean column inventory changes in anthropogenic carbon (mol C m^{-2} yr^{-1}) over the last decade.

	Atlantic Ocean (along 25°W)	Pacific Ocean (along 152°W)	Indian Ocean (along 90°E)
Northern Hemsphere	0. 63	0. 25	*
Southern Hemisphere	0. 75	0. 41	*

*Indian Ocean cruises are scheduled for 2007–08.

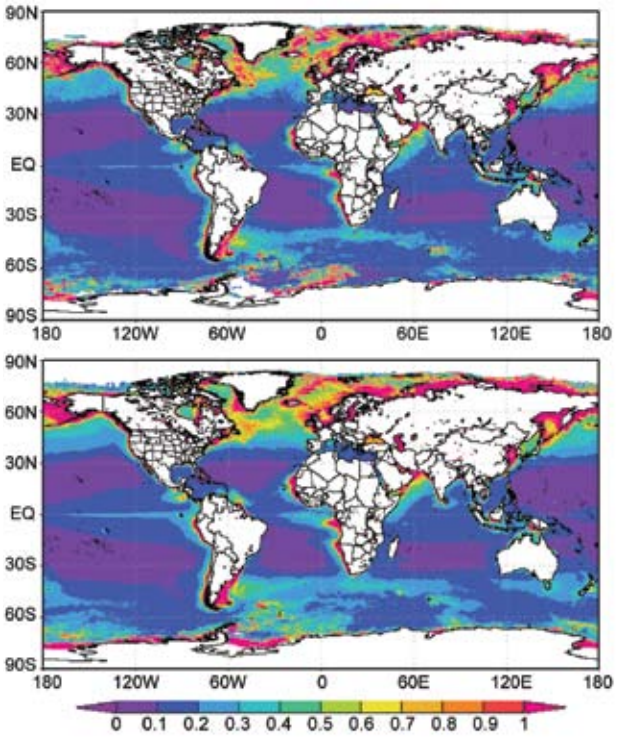

Fig. 3.20. Global time-averaged chlorophyll-a concentration (mg m^{-3}) plots for (top) January–December 2006 and (bottom) September 1997–December 2005. Images generated by NASA's Giovanni (giovanni.gsfc.nasa.gov).

Ocean color can potentially illustrate the distribution of nutrients and changes in stratification and circulation within oceanic basins. Marine phytoplankton influence the global pattern of the SST, density, and associated flows by heat release to the upper-ocean environment. Therefore, the patterns of biological production shown through ocean color can demonstrate climate changes, such as ENSO and monsoons.

Prior to the launch of satellites, global ocean color (i.e., chlorophyll-a concentration or phytoplankton biomass) datasets were nonexistent. This issue has since been eliminated with instruments such as SeaWiFS, which provides the longest historical record among all ocean color sensors. The ~9-year SeaWiFS dataset provides a means to assess the seasonal and interannual variability of ocean color on global scales. The data product used here is the NASA Goddard OBPG monthly global 9-km product, acquired using the GES-DISC Interactive Online Visualization and Analysis Infrastructure (Giovanni). The time period analyzed is from September 1997 through December 2006.

Global chlorophyll concentrations in 2006 exhibit some difference from the long-term average, but the significance of the anomalies is difficult to assess (Fig. 3.20). Low concentrations are observed in the center of ocean gyres, whereas high concentrations are detected in ocean margin waters, in equatorial upwelling regions, in river deltas, at latitudinal belts greater than approximately 40°N/S, and within the southern subtropical convergence zone (Yoder and Kennelly 2003; Behrenfeld et al. 2001). However, the elevated levels associated with riverine input should be given special consideration because the signature observed could be a result of either detritus, colored dissolved organic matter, or suspended particulate matter within the water column (Joint and Groom 2000).

Peak chlorophyll concentrations occur during spring and fall, while minimums occur during winter and summer (Yoder and Kennelly 2003; Miller 2004). Typically, the Tropics have low annual productivity, whereas the temperate and polar regions exhibit high productivity (Garrison 2005). However, phytoplankton blooms are observed in the eastern tropical Atlantic during boreal summer resulting from multiple mechanisms, one of which is the intensification of the southeast trade winds (Pérez et al. 2005). The temperate zone undergoes two peaks in phytoplankton biomass (i.e., phytoplankton blooms; Garrison 2005). The larger of these is observed during boreal spring and the smaller during boreal fall. In comparison, polar regions experience only one peak in phytoplankton biomass, which is observed during boreal summer (Garrison 2005).

A globally averaged time series of chlorophyll-a concentrations from September 1997 to December 2006 reveals low concentrations during boreal winter and an occasional dip in concentration around boreal summer (not shown). Peak chlorophyll-a concentrations are observed primarily during boreal spring (May), with an occasional increase in concentration during boreal fall. Analysis of chlorophyll-a concentration anomalies from September 1997–December 2006 depict above-normal concentrations of approximately 0.021 mg m^{-3} in August 1998 and approximately 0.034 mg m^{-3} in July 2005 (Fig. 3.21). The August peak in 1998 is a direct result of the strong 1998–2001 La Niña event that took place in the equatorial Pacific, whereas the peak in July 2005 is a combination of a highly active biological summer season in the eastern tropical Atlantic and northern polar region. Note that the depicted chlorophyll anomalies are the differences between the monthly standard mapped image product and the monthly climatology standard mapped image product from OBPG, where the climatology data are derived by time binning the monthly binned files from Septem-

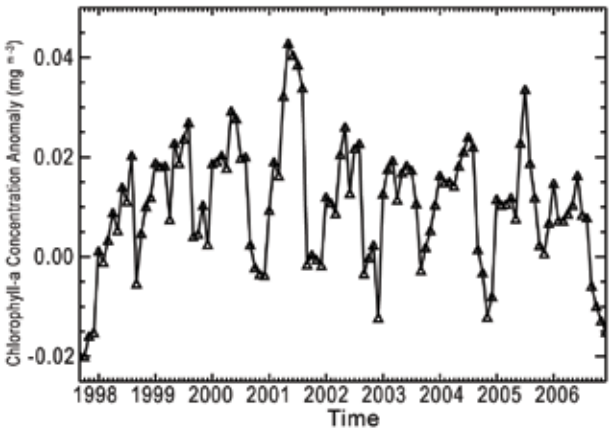

Fig. 3.21. Global area-averaged chlorophyll-a concentration anomalies (mg m^{-3}) for September 1997–December 2006.

ber 1997 through August 2006, and are mapped to an equidistant cylindrical projection with 9-km resolution at the equator. Each month is derived from nine years of monthly bins (online at http://reason.gsfc.nasa.gov/OPS/Giovanni/Readme_climate_seawifs.shtml).

Other anomalies to highlight are the above-normal chlorophyll concentration of approximately 0.043 mg m^{-3} in May 2001 and below-normal concentration of approximately –0.02 mg m^{-3} in the boreal fall of 1997 (Fig. 3.21). The below-normal concentrations in 1997 are a direct result of the extremely strong 1997/98 El Niño event. The peak in May 2001 is attributed to the negative state of the NAO. When the NAO index is negative, phytoplankton biomass and productivity in the North Atlantic have higher-than-mean conditions because of enhanced winter mixing of subtropical waters (Yoder and Kennelly 2003; Follows and Dutkiewicz 2002).

El Niño and La Niña events alter the previously described seasonal cycle of phytoplankton stocks in the Northern Hemisphere. Peak concentrations are observed during boreal summer in La Niña events and minimal concentrations occur during boreal fall in El Niño events. Several studies have been conducted in regard to the central/eastern equatorial Pacific chlorophyll decrease during the 1997/98 El Niño and the increase during the subsequent La Niña (Murtugudde et al. 1999; Chavez et al. 1998, 1999; Wilson and Adamec 2001; Ryan et al. 2002). Each of these studies illustrate that during a La Niña event, trade wind intensification prompts thermocline and nutricline shoaling, which increases the nutrient flux to the surface layer, generating intense phytoplankton blooms; conversely, during an El Niño event the thermocline and nutricline deepen, which impinges upwelling and reduces the supply of nutrients into the euphotic zone, thereby limiting chlorophyll production.

The year 2006 marked the beginning of the 2006/07 El Niño event. Both the 1997/98 and 2002/03 El Niños exhibited their lowest chlorophyll concentrations during the month of December. For the 2006/07 El Niño it is yet to be known at the time of writing whether peak below-normal concentrations do in fact occur in December. However, it is safe to say, based upon the available chlorophyll data, that the 2006/07 El Niño is stronger (in terms of its effects on chlorophyll) than the 2002/03 El Niño (with a below-normal concentration of approximately –0.031 mg m^{-3} in December 2006 in the Niño 3.4-region compared to approximately –0.024 mg m^{-3} in December 2002), but is less intense than the strong El Niño of 1997/98, which had a below-normal concentration of approximately –0.09 mg m^{-3} in December 1997 in the Niño 3.4-region.

4. THE TROPICS—H. J. Diamond

a. Overview—H. J. Diamond

This Tropics section consists of global input on the following three primary topics: 1) ENSO and the tropical Pacific, 2) TC activity for the 2006 season in seven basins (the Atlantic, northeast Pacific, northwest Pacific, North and South Indian, South Pacific, and Australia), and 3) ITCZ behavior in the Pacific and Atlantic basins.

The year was characterized by a transition from La Niña conditions in the first quarter of the year to El Niño conditions during the last quarter of the year. Regarding TC activity, the 2006 Atlantic season was much different than the 2005 season as follows: the number of storms dropped from 28 in 2005 to 10 in 2006, the northeast Pacific was a bit more active than in 2005, and the Australian basin had several strong storms.

b. ENSO and the tropical Pacific—G. D. Bell and M. S. Halpert

1) Overview

El Niño and La Niña episodes represent opposite phases of ENSO. These episodes are often defined from a time series of area-averaged SST anomalies in the Niño-3.4 region (called the Niño-3.4 index), which spans the central and east-central equatorial Pacific between 5°N–5°S and 170°–120°W. During 2006, this index showed below-average SSTs associated with La Niña during January–March, followed by a return to near-average temperatures and ENSO-neutral conditions during April–July (Fig. 4.1).